Reaction Chemistry & Engineering

ROYAL SOCIETY OF CHEMISTRY

PAPER

View Article Online
View Journal | View Issue

Cite this: *React. Chem. Eng.*, 2026, 11, 148

Design, characterisation and application of a miniaturised CSTR for reaction kinetic studies using *in situ* Raman spectroscopy: imine synthesis as a case study

Eleni Grammenou, [a] Andrea Friso, [a] Simon Dawes, [b] Nicholas Snead, [a] Georgios Gkogkos, [a] Maximilian O. Besenhard, [a] Maria Mourkou, [a] Federico Galvanin *[a] and Asterios Gavriilidis *[a]

Received 31st March 2025,
Accepted 2nd September 2025

DOI: 10.1039/d5re00144g

rsc.li/reaction-engineering

Magnetically agitated miniaturised continuous stirred tank reactors (m-CSTRs) are an attractive tool for the investigation of reaction kinetics, as they combine active stirring with enhanced heat and mass transfer due to their small dimensions, while their compatibility with *in situ* spectroscopic techniques enables reaction monitoring and high-throughput data acquisition. This study presents the development of a 2.65 mL m-CSTR, integrated with *in situ* Raman spectroscopy for real-time kinetic data acquisition in continuous flow. The reactor, featuring a temperature-controlled stainless-steel chamber with a top quartz glass window and a PTFE slotted impeller, was assessed for its macro- and micromixing characteristics at flowrates between 0.5 and 4 mL min^{-1}. The slotted impeller led to near-ideal CSTR behaviour and improved micromixing quality in comparison to conventional cross stir bars of similar dimensions. Using the imine synthesis of *n*-benzylidenebenzylamine from benzaldehyde and benzylamine as a model reaction, kinetic parameters were determined with direct composition measurement inside the reactor and the most informative region of the design space, *i.e.*, the experimental conditions that provide the most useful data for accurate kinetic parameter estimation and model validation, was identified to be in the region of high reactant concentrations and short residence times within the temperature range investigated (15–45 °C).

1. Introduction

Delivering high quality products at reduced costs *via* greener processes necessitates the extraction of quantitative chemical synthesis information, which involves developing precise reaction kinetic models essential for process design and optimisation. The application of micro and milli-scale reactors for developing kinetic models in continuous flow processes has been extensively demonstrated.[1–10] The integration of *in situ* and operando spectroscopic techniques marks a paradigm shift in real-time reaction monitoring. It enables rapid qualitative and quantitative analysis of the various reaction species and provides a reliable alternative to well-established online analytical techniques, such as High Performance Liquid Chromatography (HPLC) or Gas Chromatography (GC) that are typically associated with time consuming procedures.[11–13]

Raman spectroscopy allows fast, contact-free, non-destructive sampling with high chemical specificity. Importantly, water does not produce Raman signals in the spectral regions where organic compounds typically exhibit peaks, enabling organics detection without water interference.[14] Although traditionally associated with qualitative analysis, Raman spectroscopy is effective in quantitative applications by leveraging the proportionality between the intensity of an analyte band and its concentration.[15] The recent advances in Raman process spectrometers, equipped with flow cells and contactless probes, enhance their seamless integration into flow processes. Schwolow *et al.*[16] demonstrated the use of a contactless Raman probe to study the kinetics of 3-piperidino-propionic acid ethyl ester synthesis in an aluminium plate microreactor under steady and transient conditions. Cao *et al.*[17] employed a silicon-glass microreactor system with four micro-packed beds to investigate the multiphase oxidation of benzyl alcohol, using a portable Raman spectrometer, thereby highlighting the application of operando Raman spectroscopy for catalyst evaluation. Both studies demonstrate the use of intricate channel geometries

[a] *Department of Chemical Engineering, University College London, Torrington Place, London, WC1E 7JE, UK. E-mail: f.galvanin@ucl.ac.uk, a.gavriilidis@ucl.ac.uk*
[b] *Workshop of Biochemical Engineering, Chemical Engineering and Physics, University College London, Torrington Place, London, WC1E 7JE, UK*

in microfluidic chip reactors, which allow for measurement at multiple locations, a feature particularly useful for fast reactions. However, for reactions requiring longer residence times, necessary adjustments to the microchannel lengths could result in increased pressure drop and extended time and material consumption to reach steady state. To address this challenge, Klement *et al.*[18] introduced a novel sandwich minichannel reactor for oscillating droplets that enabled Raman spectroscopy to analyse individual droplets within a PTFE channel. The same group further streamlined this reactor design, applying it to study the kinetics of acrylic acid polymerisation in slug flow.[19] Schulz *et al.*[20] also employed this reactor setup to investigate the kinetics of imine synthesis, coupling Raman spectroscopy with chemometrics.

Miniaturised continuous stirred tank reactors (m-CSTRs) provide an alternative that merges the small footprint and reagent efficiency of microreactors with the active mixing and back-mixing characteristics of conventional CSTRs. With volumes of a few millilitres, m-CSTRs are well-suited for solid-producing reactions,[21–23] synthesis of nanoparticles,[24–26] multiphasic flow chemistry[27,28] and investigation of slower reactions.[29] A key advantage of m-CSTRs lies in their operational versatility, an aspect that is particularly useful for reaction kinetic studies. When operated in continuous flow, they enable the collection of steady-state data under precisely controlled conditions. Incorporating transparent windows allows for integration with non-invasive spectroscopic tools, such as *in situ* Raman (using quartz windows) and transflectance IR spectroscopy (using CaF_2 windows). This capability would be valuable for high-throughput kinetic screening, automated experimentation, and process development.[30–32] In contrast to many microreactor formats that are limited to continuous flow, m-CSTRs can also be adapted for batch operation with minimal modifications. However, batch operation in conjunction with real-time spectroscopic monitoring would generally be better suited for slower reaction systems. For fast reactions, a significant portion of conversion can occur during the initial filling or mixing phase before accurate sampling and data collection can begin. This "dead time" at the start of the experiment would make it difficult to accurately capture the initial kinetics with spectroscopic techniques. This issue may not arise in all systems; Guan *et al.*[33] reported batch studies on multiphasic reactions with online pressure measurement. However, offline analysis was ultimately preferred for accurate concentration measurements.

Despite the clear promise of m-CSTRs for kinetic investigations, especially in continuous operation, no prior reports have demonstrated their use for acquiring continuous flow kinetic data using *in situ* spectroscopy. Our work introduces a temperature-controlled m-CSTR, equipped with a Raman spectrometer probe that analyses the reaction mixture inside the reactor, for real-time kinetic data acquisition. The combination of *in situ* spectroscopic monitoring and improved mixing performance at this scale, through a custom-made slotted impeller, allows our reactor to collect accurate kinetic data under steady-state operation, demonstrating a pathway for automating and streamlining kinetic analysis in flow chemistry. We begin by evaluating the mixing behaviour of the m-CSTR, assessing both micromixing and macromixing quality. We then demonstrate the reactor's capability to rapidly generate kinetic data through integration with an automated experimental platform. To validate our system, we selected a fast, homogeneous liquid-phase imine synthesis as a model reaction. This choice presents stringent demands on mixing efficiency and time-resolved spectral acquisition, providing a rigorous proof of concept for the reactor performance. Successful kinetic monitoring of this rapid reaction demonstrates the robustness of our approach and establishes a foundation for future studies involving more complex or multiphase systems.

2. Materials and methods

2.1. Reactor design and fabrication

The m-CSTR designed for this work consists of the following five main components:

1. Reactor chamber: Constructed from 316 stainless steel, the cylindrical chamber has an internal diameter of 15 mm and a depth of 15 mm, resulting in a total internal volume of 2.65 mL.

2. Optical window: A 25 mm diameter, 2 mm thick quartz optical grade window (Knight Optical) is mounted on top of the reactor chamber, providing optical access for the Raman probe.

3. Reactor lid: A 316 stainless steel lid seals the reactor chamber together with the optical window, ensuring a secure, leak-proof environment.

4. Cooling/heating jacket: Made of 316 stainless steel, the jacket has a square body (90 × 90 × 24.65 mm) with an inner protruding fin to enhance the recirculation of cooling/heating fluid.

5. Reactor cover: A 316 stainless steel reactor cover is used to minimise heat loss due to convection with the surrounding environment, maintaining stable temperature conditions within the reactor.

Two 2 mm I.D. holes were drilled at a 90° angle to each other on the side walls in close proximity to the bottom of the reactor chamber, designed for the introduction of the reactants. A 2 mm I.D. hole, used as the outlet, was drilled on the side wall, 4 mm below the top of the reactor chamber, to minimise short-circuiting of the reacting mixture. A custom-made slotted impeller with dimensions of 8 mm in height and 13 mm in diameter was designed and fabricated from PTFE. The impeller featured a pocket for fitting a high-pull rare earth magnet to enable coupling with an external magnetic stirring unit to control the impeller's rotational speed. Its asymmetric design consisted of four arms containing a set of fins, separated by narrow slots (gaps) to enhance mixing. The volume of the impeller without the magnet was 0.24 mL and 0.30 mL including the magnet. As such, when inserted into the reactor (total internal volume: 2.65 mL), the effective working volume was reduced to 2.35 mL. All the reactor components, including the impeller, were machined using CNC milling (Haas TM1P Vertical

Machining Centre). The whole unit has the capability to withstand harsh chemical environments, and the integration of a heating jacket allows conducting reactions at the desired temperature by connecting it with a circulating bath. Further details on the design and fabrication of the reactor system can be found in the SI, S1. Fig. 1 shows the CAD model, a picture of the fully assembled reactor and an exploded view of the reactor. For the investigation of micromixing performance of the PTFE custom-made slotted impeller, a PTFE cross-stir bar of 10 mm in diameter and 5 mm in height (total volume of 0.18 mL) was also employed for comparison.

2.2. Reactor characterisation

2.2.1. Residence time distribution (RTD). To characterise the macromixing behaviour of the m-CSTR and quantify deviations from ideal behaviour, such as dead volume and bypass, the RTD of the m-CSTR unit was obtained using the step injection method, as shown in Fig. 2a. The carrier phase was deionised (DI) water, and the tracer was a solution of methylene blue (0.0085 mg mL^{-1}, Basic Blue 3, Sigma Aldrich) with a maximum UV-vis absorbance peak of ~0.8 at 652 nm. Prior to the RTD study, the concentration of methylene blue was correlated with its UV-vis peak absorbance at the same wavelength revealing a linear relation between concentration and absorbance in the investigated region. Two syringe pumps (Hamilton) were used to pump the blue dye solution and DI water through a four-way valve (IDEX, 4 port manual switch valve) in one of the m-CSTR inlets, while keeping the other one blocked, to achieve a step tracer input. The reactor was stirred by adjusting the stirring speed in a digital hotplate-stirrer (RCT 5 digital, IKA). Flowrates similar to the reaction kinetic experiments were used ranging from 0.25 to 4 mL min^{-1} and stirring speeds of 250, 500 and 1000 rpm were investigated. A custom, no-contact flow cell was employed,[34] where a transparent FEP outlet tube with an optical path length of 0.7 mm (determined by comparing the UV-vis absorption of a known solution in a standard 1 cm optical path length cuvette) was positioned perpendicular to the optical fibres for direct measurement of the fluid absorbance at the reactor outlet. The absorbance was measured using a UV-vis spectrometer (USB2000+, Ocean Optics) with a deuterium-halogen light source (Ocean Optics). The DI water background was subtracted before the experiment. The integration time was set to 30 ms and scans were taken approximately every 1 s. Each experiment was repeated at least twice, interchanging the inlet stream between the two available reactor inlets to ensure that the results were independent of the inlet position and to account for the effect of potential faults in the fabrication procedure of the m-CSTR. The differences in the obtained data were negligible.

The concentration was normalised, based on the maximum concentration of the tracer injected. Short sections of tubing were used to connect the inlet of the reactor to the four-way valve and the outlet of the reactor to the flow cell. Despite their relatively short lengths, the outlet concentration profile of the system was a convolution of the RTD of the reactor and the connecting tubings. To obtain only the m-CSTR's RTD, an additional RTD experiment was performed connecting the inlet and outlet tubing sections directly, to evaluate their contribution to the system's output.

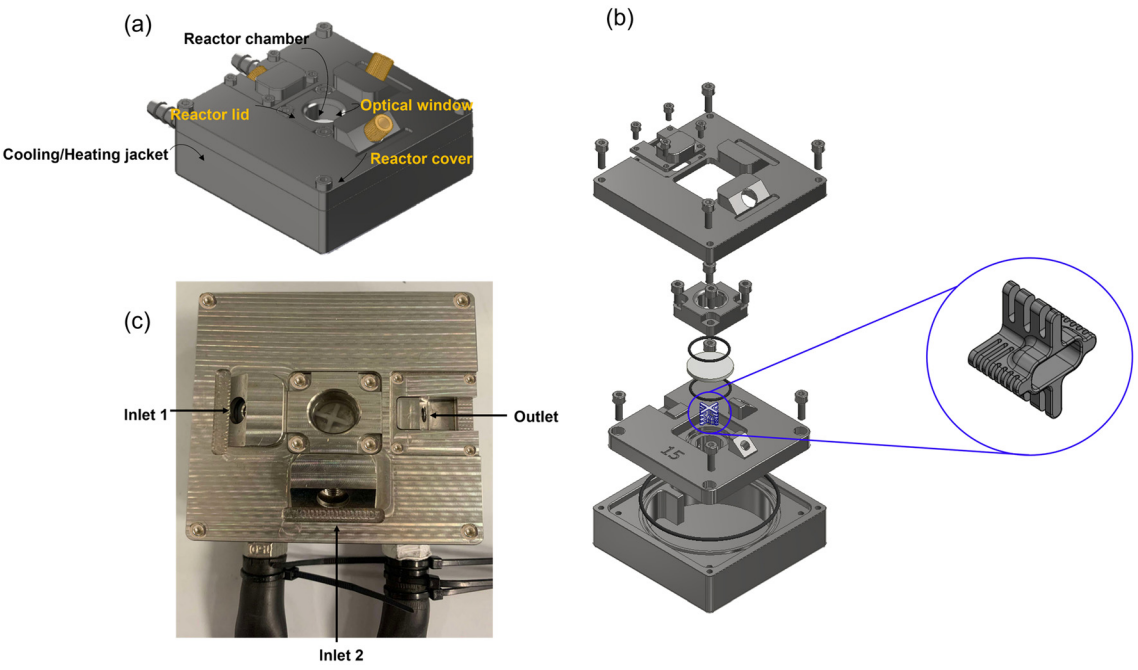

Fig. 1 (a) CAD design of m-CSTR, (b) exploded reactor assembly, with a zoomed-in detail of the custom-designed slotted impeller and (c) picture of assembled m-CSTR.

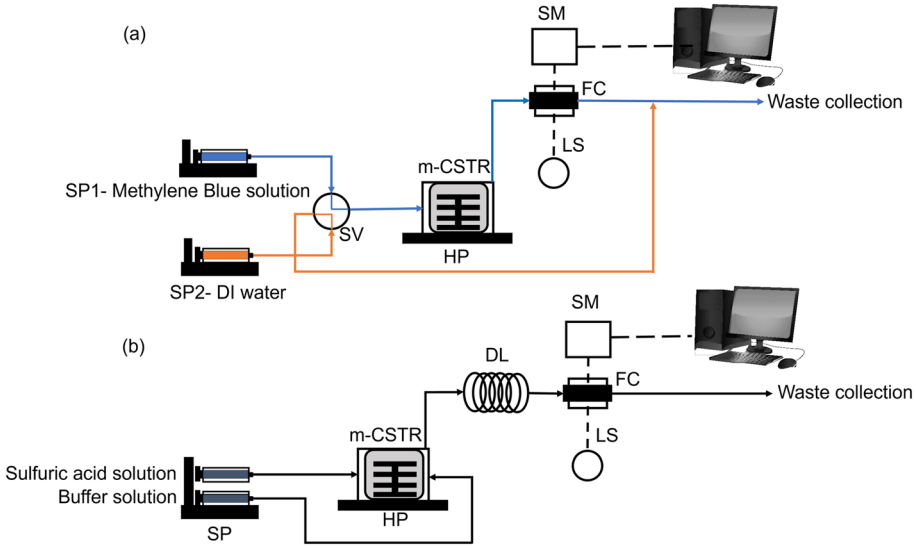

Fig. 2 (a) Experimental set-up for the residence time distribution (RTD) studies (orange lines indicate the DI water flow and blue lines indicate the blue dye flow), (b) experimental set-up for the micromixing studies using the Villermaux–Dushman reaction. SP: syringe pump, SV: switch valve, SM: UV-vis spectrometer, FC: flow cell, LS: light source, DL: delay loop, HP: hotplate-stirrer, m-CSTR: miniaturised CSTR.

Fast Fourier transform (FFT) and smoothening of the data using the Savitzky–Golay filter were used for deconvolution of the signal.[35] A detailed description of the data post-treatment can be found in Gkogkos *et al.*[25] and the SI (section S5). The normalised deconvoluted RTD function of the reactor E_θ was compared with that of the ideal CSTR model $E_{\theta,\mathrm{model}}$ (eqn (1)) by evaluating the coefficient of determination, R^2, between the experimental and the model RTD curves (eqn (2)).

$$E_{\theta,\mathrm{model}} = \mathrm{e}^{-\theta} \tag{1}$$

$$R^2 = 1 - \frac{\sum_{\theta=0}^{4.5} \left(E_\theta - E_{\theta,\mathrm{model}}\right)^2}{\sum_{\theta=0}^{4.5} \left(E_\theta - \overline{E}_\theta\right)} \tag{2}$$

where, $\theta = t/\tau$ is the normalised residence time, t is the absolute time, $\tau = Q/V_\mathrm{R}$ is the space time of the reactor, Q is the volumetric flowrate entering the reactor and V_R is the total free volume of the reactor (after subtracting the volume of the impeller). $\overline{E}_\theta$ is the average of the experimental values E_θ over the range $\theta = 0 - 4.5$.

2.2.2. Micromixing. To quantify the performance efficiency of micromixing, the Villermaux–Dushman rapid parallel competitive reaction system was used[36] (eqn (3) and (4)). The reaction system involves the addition of sulfuric acid (3 M stock solution, Alfa Aesar) to a buffer solution containing a mixture of orthoboric acid (99.5% Sigma-Aldrich), sodium hydroxide (2 M, Sigma-Aldrich), potassium iodide (99%, Sigma-Aldrich), and potassium iodate (98% Sigma-Aldrich) ions.

$$H_2BO_3^- + H^+ \leftrightarrow H_3BO_3 \tag{3}$$

$$5I^- + IO^{3-} + 6H^+ \leftrightarrow 3I_2 + 3H_2O \tag{4}$$

The acid–base neutralisation reaction (eqn (3)) and the redox reaction (eqn (4)) are competitive reactions for the available protons supplied by the sulfuric acid, with the former being quasi-instantaneous and the latter being rapid, but with a significantly lower reaction rate than that of the neutralisation reaction. When micromixing is not instantaneous, the redox reaction proceeds due to incomplete consumption of protons, resulting in the generation of iodine. The generated iodine from the redox reaction reacts further with excess iodide to reversibly generate triiodide ions, as shown in eqn (5).

$$I_2 + I^- \leftrightarrow I_3^- \tag{5}$$

The triiodide formed has a distinct yellow colour and a strong UV-vis absorption peak at the wavelength of 353 nm and can be quantified using the Beer–Lambert law, as presented in eqn (6).

$$C_{I_3^-} = \frac{\mathrm{OD}}{\varepsilon_{353} l_\mathrm{optical}} \tag{6}$$

where, $C_{I_3^-}$ is the concentration of triiodide, OD denotes the optical density, ε_{353} the extinction coefficient of triiodide at 353 nm (23 209 L mol^{-1} cm^{-1} [37]) and l_optical the optical path length within the measurement cell.

The degree of micromixing efficiency can be quantitatively described by the segregation index X_S, and the mixing time, t_m. Both parameters' estimation is relying on the selection of a mixing model, able to describe the mechanistic properties of the integration of the two fluid streams. The segregation index X_S is defined as

$$X_S = \frac{Y}{Y_{ST}} \quad (7)$$

where, Y is the ratio of acid mole number consumed by the redox reaction (eqn (4)) divided by the total acid mole number injected and Y_{ST} is the value of Y when the mixing process is infinitely slow, *i.e.* the neutralisation reaction (eqn (3)) and the redox reaction (eqn (4)) become quasi-instantaneous compared to the mixing time, t_m. X_S, which ranges from 0 to 1, equals 0 under conditions of perfect micromixing and 1 at total segregation, respectively.

In this work, the concentrations proposed by Commenge and Falk[38] for set 1c were used. The correlation between the mixing time and the triiodide concentration (or equivalently the segregation index, X_S) was established by specifying the initial reagent concentrations and solving the Interaction by Exchange with the Mean (IEM)[39,40] model for various mixing times (see SI, S6).

For the micromixing analysis, the prepared acid and buffer solutions were loaded separately in 100 mL syringes (SGE) and were pumped simultaneously by the same syringe pump (PHD ULTRA, Harvard) (Fig. 2b). The reactor was stirred by adjusting the rotational speed in a digital hotplate-stirrer (RCT 5 digital, IKA). Flowrates similar to the RTD and reaction kinetic experiments were used, ranging from 0.5 to 4 mL min^{-1} and stirring speeds of 250, 500, 750 and 1000 rpm were investigated. The outlet of the m-CSTR was connected to the UV-vis analysis set-up by 1 m long PFA tubing (delay loop) to ensure that the reactions were completed and equilibrated. The triiodide concentration was monitored at 353 nm, using the same UV-vis system, as in the RTD experiments (section 2.2.1) but with optical fibres (200–1100 nm, Ocean Optics) optimised for transmission in the UV region. The experiments were repeated three times with the two reactant streams swapped between the inlets, and no differences were observed in the obtained data.

2.3. Reaction kinetics experiments

2.3.1. Reaction and experimental set-up. To demonstrate the ability of the m-CSTR to precisely estimate kinetic parameters *via* Raman spectroscopy, a well-understood chemistry where the reagents and products are Raman active was selected; the synthesis of *n*-benzylidenebenzylamine from benzaldehyde (ReagentPlus, 99%, Sigma-Aldrich) and benzylamine (ReagentPlus, 99%, Sigma-Aldrich) in methanol (>99%, Fischer Scientific), as shown in Fig. 3.

The synthesis of *n*-benzylidenebenzylamine follows second order kinetics[20,41,42] (eqn (8)).

$$-r_{BAl} = kC_{BAl}C_{BAm} \quad (8)$$

where, k is the reaction rate constant, C_{BAl} is the concentration of benzaldehyde and C_{BAm} is the concentration of benzylamine. Feeding the two reactants in a stoichiometric ratio of 1 : 1, allows for the simplification of the reaction rate to eqn (9).

$$-r_{BAl} = kC_{BAl}^2 \quad (9)$$

Fig. 4 provides a simplified schematic representation of the experimental set-up. Two glass syringes (25 mL each, CETONI) were separately filled with a solution of benzaldehyde in methanol and benzylamine in methanol (2 M each). Another glass syringe (25 mL, CETONI) was filled with methanol and acted as the dilution stream for one of the reactants. Dilution of only one of the streams was sufficient to achieve equal inlet concentrations of both reactants. All syringes were mounted on a Nemesys medium-pressure syringe pump (CETONI). The inlet concentrations of benzaldehyde and benzylamine entering the reactor were determined by the relative pump flowrates. Mixing in the reactor was achieved by adjusting the stirring speed of the magnetic hotplate-stirrer. To ensure isothermal operation, the feed streams were preheated using a digital magnetic hotplate-stirrer (RCT 5 digital, IKA), while a cooling/heating circulator (CC-K6, Huber) was connected to the reactor's jacket ports, allowing water recirculation with adjustable temperature. The reaction temperature was controlled by a type K thermocouple (RS PRO) that was inserted into the reaction chamber through a T-junction (IDEX), located at the outlet of the reactor. This thermocouple was connected to an Arduino control box and provided the set-point that was used to adjust the water bath temperature through a PID control script (see SI, S3). The reaction mixture exiting the reactor was collected into a waste vessel (Festo). To prevent evaporation of the solvent, the entire system was pressurised to 1 barg with nitrogen (BOC) using a mass flow controller (SLA5850, Brooks), a gas pressure sensor (40PC, 250 psig, Honeywell) and a back-pressure regulator (K series, 250 psig, Swagelok) connected to the waste vessel. The back pressure regulator ensured that the pressure in the waste vessel was no lower than a certain value, while also working as pressure relief valve, expelling excess gas. One pressure relief valve (U-456, 100 psi, IDEX) was installed right after the reactor outlet to avoid overpressure above 7 bar, as the glass syringes used could withstand up to 10 bar.

The experimental process was automated using the Laboratory Virtual Instrument Engineering Workbench (LabVIEW) environment.[43] The LabVIEW code allowed the user to run a set of experiments by setting the temperature, feed concentrations and total flowrate at the user interface panel. For visualisation purposes, the temperature and

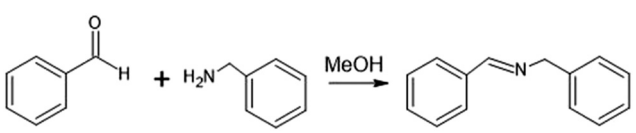

Fig. 3 Imine synthesis employed as a test reaction for the m-CSTR coupled with Raman spectroscopy.

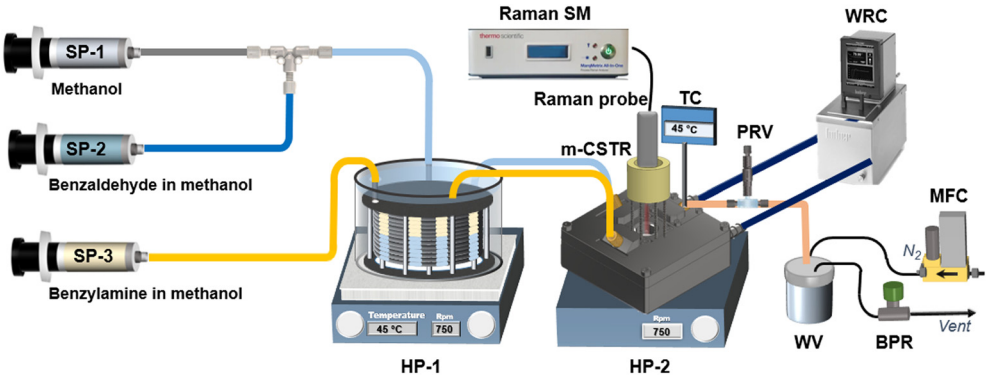

Fig. 4 Experimental set-up for the kinetic data acquisition of the *n*-benzylidenebenzylamine synthesis. SP: syringe pump SM: spectrometer, PRV: pressure relief valve, WRC: water circulator, HP: hotplate-stirrer, MFC: mass flow controller, TC: thermocouple, WV: waste vessel, BPR: back pressure regulator, m-CSTR: miniaturised CSTR. HP-2 was only used as a stirrer. All temperature, pressure and flow equipment were controlled by LabVIEW.

pressure trends of the system were also displayed in real time in graph charts. The code featured overheating and overpressurisation safety limits, which were set to 80 °C (to prevent evaporation in the water circulator) and 2 barg respectively and would automatically stop the experiment if these values were exceeded.

2.3.2. *In situ* Raman analysis. The Raman probe (all-in-one with BallProbe, laser wavelength 750 nm, MarqMetrix) was mounted in a 3D-printed in-house fabricated holder for reproducible sampling (see SI, S2). The probe tip was positioned approximately 2 mm away from the outer surface of the 2 mm-thick quartz window, placing the focal point around 4 mm from the probe tip, within the reaction mixture. No noticeable fluctuations in Raman signal intensity were observed due to the rotation of the slotted impeller. The integration time was set to 500 ms, and the laser power was set to 300 mW. The Raman spectra were recorded continuously as a function of time until no further spectral changes were observed, indicating that steady state had been reached. This typically occurred after 3–5 residence times. The final five measurements taken after this point were considered representative of the steady-state condition, each comprising an average of 10 scans.

The concentration of the reactants and products was calculated based on the area of the peak corresponding to the characteristic C═O stretching of benzaldehyde at 1680–1730 cm^{-1} and C═N stretching of *n*-benzylidenebenzylamine at 1630–1670 cm^{-1} (benzylamine does not display distinctive peaks), as shown in Fig. 5. Prior to this, the calibration curves for the respective compounds were obtained (see SI, S4). Since Raman spectra often contain baseline drift and random noise, baseline correction was an important step to extract the correct Raman peak intensities for quantitative analysis. To address this, a MATLAB script containing the airPLS algorithm[44] was employed that provided a simple and fast estimation of the baseline, requiring the tuning of only a single parameter to ensure baseline smoothness across all recorded spectra with emphasis on the peaks of interest (see SI, S4). The carbon balance was evaluated in all experiments, yielding an average error of approximately 3% and a maximum error of 5%.

2.4. Modelling and parameter estimation

2.4.1. Design equation for a m-CSTR. An isothermal CSTR with constant volumetric flowrate for a second order reaction with equal reactant concentrations operating in steady state can be modelled using eqn (10).

$$\frac{C_{BAl,0} - C_{BAl}}{\tau} - kC_{BAl}{}^2 = 0 \quad (10)$$

where, $C_{BAl,0}$ is the concentration of benzaldehyde in the combined inlet stream. To calculate the kinetic parameters, the mass balance for *n*-benzylidenebenzylamine was also considered, hence making use of product concentration measurements, to improve kinetic parameter accuracy.

2.4.2. Parameter estimation. The primary objective of this work was to accurately determine the reaction rate constant, *k*. To achieve this, *k* was expressed in the reparametrised

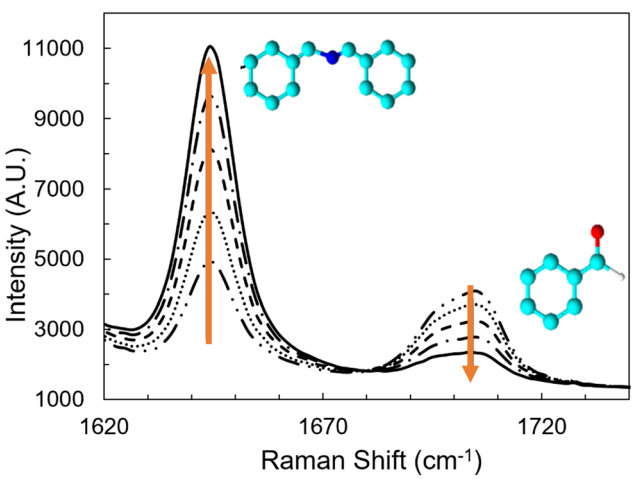

Fig. 5 Recorded Raman spectra of benzaldehyde (right peak) and *n*-benzylidinebenzylamine (left peak) as a function of residence time, τ. Arrows indicate decreasing flowrates, *i.e.* increasing residence time.

Arrhenius form with two parameters KP_1 and KP_2, as shown in eqn (11)–(14).[45]

$$k = k_{\text{ref}} \exp\left(-\frac{E_\alpha}{R}\cdot\left(\frac{1}{T}-\frac{1}{T_{\text{ref}}}\right)\right) \tag{11}$$

$$k = \exp\left(-KP_1 - \frac{KP_2\times 10^4}{R}\left(\frac{1}{T}-\frac{1}{T_{\text{ref}}}\right)\right) \tag{12}$$

$$k_{\text{ref}} = \exp(-KP_1) \tag{13}$$

$$E_\alpha = KP_2 \times 10^4 \tag{14}$$

Here, T is the reaction temperature (K), T_{ref} is the reference temperature (K), calculated as the average value of the upper and lower temperature limits of the experimental conditions and R is the ideal gas constant (8.314 J mol^{-1} K^{-1}).

The parameters were estimated by maximising the log-likelihood function (see SI, S10). The results of the parameter estimation for KP_1 and KP_2 were analysed in terms of estimated values and statistics to quantify both the precision of the estimates and model's goodness of fit. Precision was assessed using Student's t-test statistics; the t-value at the 95% confidence level of each kinetic parameter should exceed the tabulated reference t-value given by a Student t-distribution.[46] Model fitting quality was evaluated using chi-square (χ^2) statistics, where the χ^2 value should be lower than the 95% reference value from statistical tables for the correct number of degrees of freedom.[47] An information analysis was carried out to quantify the relative amount of information distributed across different experiments, through the evaluation of the Relative Fisher Information (*RFI*).[48,49] This distinction is particularly valuable, as it highlights which data points are the most informative within the experimental framework.

The analysis was performed by first computing a metric derived from the Fisher Information Matrix (*FIM*), an $N_\theta \times N_\theta$ matrix that quantifies the amount of information that can be obtained from a single experiment. The *FIM* ($\hat{\mathbf{H}}_\theta$) was evaluated using the set of experimental conditions denoted by $\boldsymbol{\varphi}$, at the estimated values $\hat{\boldsymbol{\theta}}$ of the model parameters:

$$\hat{\mathbf{H}}_\theta\left(\hat{\boldsymbol{\theta}},\boldsymbol{\varphi}\right) = \left[\hat{\mathbf{H}}_\theta^0 + \sum_{k=1}^{N_{\text{exp}}}\sum_{i=1}^{N_y}\sum_{j=1}^{N_y}\left(\frac{\partial\hat{y}_i(t_k)}{\partial\hat{\theta}_l}\,\Sigma_{ij}^{-1}\,\frac{\partial\hat{y}_j(t_k)}{\partial\hat{\theta}_m}^T\right)_{l,m=1,\ldots,N_\theta}\right] \tag{15}$$

In eqn (15), $\hat{\mathbf{H}}_\theta$ represents the global information obtained from the experiment, Σ_{ij}^{-1} is the ij-th element of the inverse covariance matrix of measurement errors, while $\hat{\mathbf{H}}_\theta^0$ is the prior Fisher information matrix. $\hat{y}_i$ refers to the prediction of the i-th concentration at the sampling time t_k.

The *RFI* was then evaluated based on the *FIM*.[48,49]

$$RFI_{ij} = \frac{\left\|\mathbf{H}_{ij}\right\|}{\sum_{i=1}^{N_{\text{exp}}}\left\|\mathbf{H}_{ij}\right\|} = \frac{\left\|\mathbf{H}_{ij}\right\|}{\left\|\mathbf{H}_j\right\|} \tag{16}$$

where $\|\mathbf{H}_{ij}\|$ represents a norm of the FIM for the i-th experiment and the j-th parameter, as computed from eqn (15), and $\|\mathbf{H}_j\|$ denotes a norm of total information obtained from the N_{exp} experiments for the identification of the kinetic model parameters. The norm $\|.\|$ can be selected based on different criteria, such as the determinant, the maximum eigenvalue, or the trace of the *FIM*. In this work, the trace of the *FIM* has been employed as the chosen norm.

The standard deviation of the measurement error for each response variable (concentration of benzaldehyde, C_{BAl} and concentration of *n*-benzylidenebenzylamine, C_{BIm}), was calculated using the method of pooled standard deviation[50] from repeated identical experiments to be 0.017 M for benzaldehyde and 0.014 M for *n*-benzylidenebenzylamine, respectively. These standard deviations were used to calibrate the constant variance model for parameter estimation and model adequacy evaluation (see SI, S10). The measurement error was attributed to the Raman spectrometer used in an open beam configuration that can be considered more sensitive to variations in the surrounding environment than a spectroscopic flow cell.

2.4.3. Experimental design. A factorial design (FD) using three factors (flowrate, temperature and inlet concentration of benzaldehyde) with two levels per factor was employed, which resulted in 8 experimental conditions. Additionally, a mid-range temperature was investigated to confirm the validity of the model bringing the total number of experimental conditions to 12 (see SI, S9). The bounds of the design space were dictated by constraints in the experimental platform. Residence times were constrained by the accuracy range of the syringe pumps, which applied pressure on 25 mL glass syringes, dispensing through the system under 1 barg backpressure and by the rate of syringes emptying. It was experimentally found that the 25 mL glass syringes could not pump accurately below 80 μL min^{-1}, therefore the lower inlet flowrate investigated was chosen equal to 0.5 mL min^{-1}. The higher flowrate for completion of the experiments within one experimental cycle without the need for a refill was 2 mL min^{-1}. The reaction temperature range was determined based on the boiling point of methanol (64.7 °C at 1 atm) and the cooling/heating ability of the water circulator, where water was used as the heat exchange medium. The minimum and maximum temperatures were set at 15 °C and 45 °C, respectively. The investigated design space is presented in Table 1. The same campaign of experiments was conducted in three replicates on three consecutive days, thus allowing to establish the robustness and reproducibility of the system.

Table 1 Boundaries of the control variables in steady-state experimentation

Control variable	Lower limit	Upper limit
Flowrate (mL min^{-1})	0.5	2
Temperature (°C)	15	45
Inlet concentration of benzaldehyde (M)	0.5	1

3. Results and discussion

3.1. RTD and micromixing evaluation

To compare the macromixing of the m-CSTR with the slotted impeller to perfectly mixed conditions, the RTD of the tracer in the m-CSTR was investigated at different stirring speeds (N = 250, 500 and 1000 rpm) and inlet flowrate (Q = 0.25, 1 and 4 mL min^{-1}). Fig. 6 presents the normalised RTDs, E_θ, plotted against the normalised residence time, θ, and compares them to the ideal CSTR model. In all studied cases, the system exhibited near-ideal CSTR behaviour. The influence of the inlet flowrate, Q, was found to be more significant than that of stirring speed, N, indicating that the macromixing behaviour in the system was more sensitive to convection than to the stirrer rotation effect. This trend contrasts with the findings of Gkogkos *et al.*,[26] who studied the RTD of a 3 mL m-CSTR with a pill shaped magnetic stir bar for flowrates ranging from 2 mL min^{-1} to 60 mL min^{-1}, observing increased bypassing and deviation from ideal CSTR behaviour at higher inlet flowrates. To explore the underlying causes of this discrepancy, a computational fluid dynamics (CFD) analysis of the hydrodynamics within the m-CSTR chamber was conducted based on the Multiple Reference Frame (MRF) method (see SI, S8).[51]

In all cases, when stirring was applied, the flow field was dominated by the tangential velocity component, which is associated with the rotational motion of the impeller and showed minimal sensitivity to variations in flowrate. Considering that flowrate effects were likely to be most pronounced near the inlet and outlet, the velocity field was closely examined in these regions (see SI, Fig. S11). At a flowrate of 1 mL min^{-1}, the fluid near the inlet was driven back into a localised recirculation zone by the dominant tangential flow. This recirculation zone was absent at the higher flowrate of 4 mL min^{-1}. This effect was consistently observed at stirring speeds of 500 rpm and 1000 rpm, whereas at 250 rpm, the extent of recirculation was significantly diminished. The simulations were repeated with the impeller positioned at two different angles to investigate the discrepancies in the development of the instantaneous velocity distribution with regards to the relative position of the impeller to the inlet (as MRF captures only a moment of the impeller's rotation), revealing consistent recirculation zones for both angles. The differing behaviour observed with this specific impeller design, compared to the simpler pill shaped magnetic stir bar previously reported, may be explained as follows. It is possible that similar recirculation patterns could occur with stir bars under comparable flowrate conditions. However, in the study of Gkogkos *et al.*,[26] RTD experiments were conducted at flowrates of 2 mL min^{-1} and then increased directly to 14 mL min^{-1}, a range sufficient to induce some degree of local bypassing.

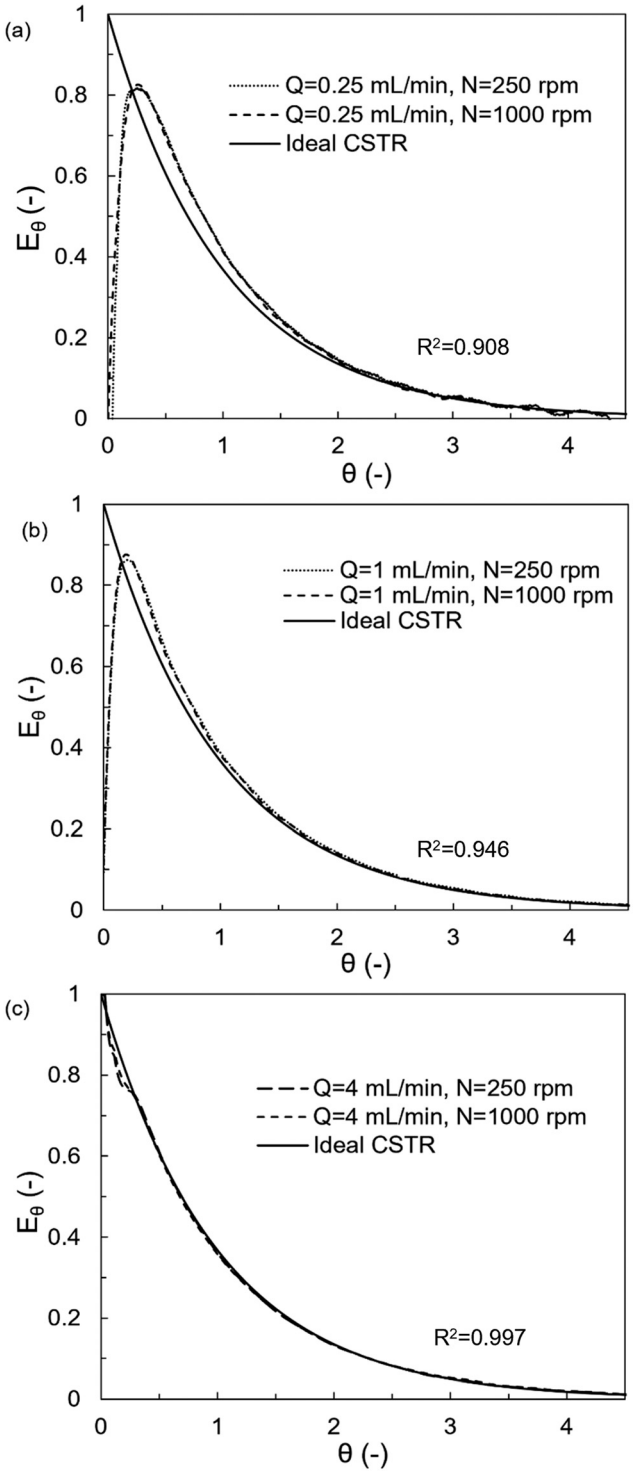

Fig. 6 E_θ curve of the m-CSTR (2.35 mL effective volume) for a total flowrate of (a) 0.25 mL min^{-1} and (b) 1 mL min^{-1} and (c) 4 mL min^{-1} at 250 and 1000 rpm compared to the ideal CSTR model, using the slotted impeller.

Furthermore, the impeller employed in this study differed significantly from the pill shaped magnetic stir bar. This custom impeller design generated a strong swirling tangential velocity profile near the impeller extremities, which progressively attenuated with distance from the impeller extremities towards the reactor wall, particularly near the top and bottom of the reactor chamber. In contrast, pill shaped stir bars produce a more localised tangential flow. Notably, the slotted impeller spans nearly the entire tank and has a larger diameter (relative to the tank size) compared to the stir bars.

Given the complex hydrodynamics resulting from the confinement of the flow within the reactor, these observations underscore the importance of the impeller design in influencing flow patterns and macromixing efficiency. As the reactor's E_θ curve showed a high degree of agreement with the ideal CSTR model ($R^2 > 0.90$) across the investigated cases, the m-CSTR was modelled as an ideal stirred reactor.

For the micromixing analysis, stirring speed between 250 and 1000 rpm and inlet stream flowrates ranging from 0.25 mL min^{-1} to 2 mL min^{-1} (total flowrate Q of 0.5 mL min^{-1} and 4 mL min^{-1}) were investigated. The slotted impeller and a cross stir bar were tested for water solutions with an acid-to-buffer solution flowrate ratio of 1. In Fig. 7a and b, the micromixing time, t_m, calculated by the IEM model[39,40] is plotted against the stirring speed for each impeller (the segregation index is reported in the SI, S7). Fig. 7a and b reveal that for both stirring configurations, micromixing time was dependent on the stirring speed, N. As the value of N increased, micromixing time for the slotted impeller and the cross stir bar tended to decrease. This can primarily be attributed to the greater energy input into the fluid and the increased velocity gradient and shearing force within the stirring unit. The decrease was sharper between 250 and 500 rpm and with a less steep gradient for $N > 500$ rpm for the flowrate range studied, showing less sensitivity to the flowrate at larger N, where the high turbulent kinetic energy dissipation dominated the micromixing process. For both impellers at N = 1000 rpm, an increase in the micromixing time was observed. This increase may result from an antagonistic effect of the inlet flow and the increased stirring rates and can also be associated with the CFD observations in the macromixing analysis. At N = 1000 rpm, the impellers completed 16.7 rotations per second, translating into 1 rotation per 6 milliseconds, a timeframe comparable to the micromixing time measured. At lower flowrates, the entering fluid had reduced kinetic energy. Localised recirculation zones formed near the inlets due to the strong swirling flow generated by the impeller. As a result, reactant molecules did not have sufficient time to diffuse and react. They were rapidly swept away from the reaction zone at the bottom of the reactor, in the space between the inlets and the impeller. This trend was less significant in the case of higher inlet velocities, based on the micromixing values for flowrates of 4 mL min^{-1}, where t_m decreased up to 750 rpm and then remained independent of the stirring speed.

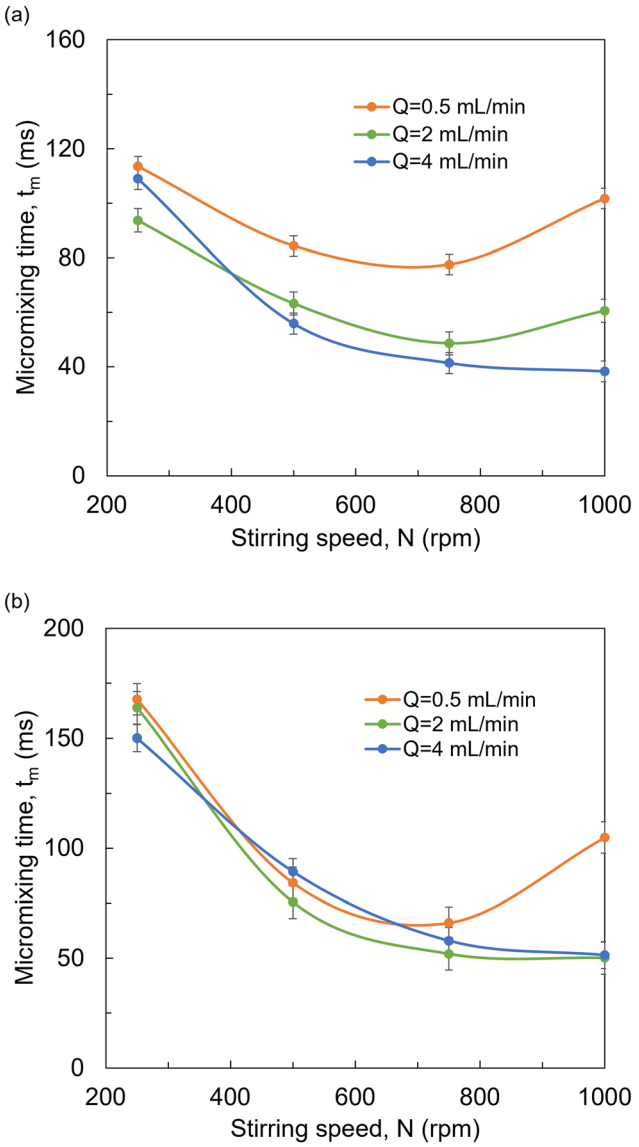

Fig. 7 Micromixing time, t_m, *vs.* stirring speed, N, for flowrates of Q = 0.5, 2 and 4 mL min^{-1} for (a) the slotted impeller and (b) the cross stir bar. Error bars are calculated based on the standard deviation of repeated experiments.

For the custom-made slotted impeller, Fig. 7a highlights the effect of the inlet flowrate on the micromixing quality. As the flowrate increased from 0.5 mL min^{-1} to 4 mL min^{-1}, micromixing times reduced significantly across all stirring speeds, with the highest flowrate of 4 mL min^{-1} consistently yielding the shortest micromixing times. In contrast, for the cross stir bar (Fig. 7b), the effect of stirring speed dominated over the convection effect of the flowrate, with a sharp increase in the micromixing efficiency evidenced by an average 43% reduction in micromixing time at stirring speeds between 250 and 500 rpm, regardless of the flowrate. Up to 750 rpm, micromixing time remained nearly the same across the range of flowrates studied, with variations within

the limits of experimental error, as indicated by the error bars. Overall, the m-CSTR unit employing the slotted impeller demonstrated satisfactory micromixing and displayed better performance across the tested inlet flowrates, compared to the conventional cross stir bar, especially for low stirring speeds.

3.2. Kinetic parameter estimation

Parameter estimation results are presented in Table 2. Parameters KP_1 and KP_2 were estimated with good precision, based on their *t*-values that were higher than the reference *t*-value and a good fitting of the experimental data to the model was granted, as the χ^2-test was amply satisfied (χ^2 = 41.21 < 48.50).

The adequacy of the 2nd order kinetic model is shown graphically in the parity plot of Fig. 8, where the model predictions for the concentration of benzaldehyde and *n*-benzylidenebenzylamine fall around the interval of the experimental standard deviation.

To evaluate the most informative experiments in the design space investigated, the *RFI*, which represents the fraction of information that each experiment is returning given the parameters KP_1 and KP_2, was computed for each experimental condition (*i.e.*, 12 different DoE points, the conditions of which can be found in Table S3 of the SI). Based on Fig. 9 that shows the *RFI* of the average of 3 replicates of 12 steady-state experimental conditions, it is evident that experiment 2 (SS2) yielded the highest *RFI* value, followed by experiments 6 (SS6) and 10 (SS10). Thus, the experimental region characterised by high reactant concentrations and short residence times (*i.e.*, high flowrate) significantly enhanced the estimation of model parameters. Conversely, experiments 1, 7 and 11 (SS1, SS7, SS11) that were carried out under (mainly) low flowrate and low inlet concentration conditions were less informative. Notably, while SS1 was performed at the lowest temperature (15 °C), SS7 and SS11 correspond to the medium (30 °C) and high (45 °C) range, suggesting that temperature alone is not the determining factor for the low *RFI* values observed. Rather, it appears that reactant concentration and residence time (flowrate) have a more dominant influence on the information content of the experiments in this system.

The estimated kinetic parameters of the imine synthesis are compared with reported values in Table 3. Fath *et al.*[42] used a coiled stainless steel microreactor of total inner volume of 1.87 mL with an *in situ* FTIR spectrometer at the end of the reactor. The kinetic data were estimated using two different approaches: previously determined calibration curves and chemometrics. Based on calibration, a reaction constant of 0.025 L mol^{-1} s^{-1} was reported at 25 °C, accompanied by an activation energy of 39.2 kJ mol^{-1}. When applying the Self-Modelling Curve Resolution (SMCR) method, the reaction rate constant varied between 0.026 and 0.065 L mol^{-1} s^{-1}, while the activation energy ranged from 41.6 kJ mol^{-1} to 43.3 kJ mol^{-1}. Schulz *et al.*[20] combined a nearly isothermal oscillating segmented flow reactor (where each 7 μL droplet behaved practically as a batch reactor) and

Table 2 Parameter estimation results for the reparametrised model including estimated values of model parameters, standard deviation of parameter estimates and 95% *t*-values

Parameter	Value	Standard deviation	95% *t*-value
KP_1	3.47	0.05	76.63
KP_2	2.75	0.28	9.81
Reference *t*-value (95%)	1.69		
χ^2 (χ_{ref}^2 = 48.50)	41.21		

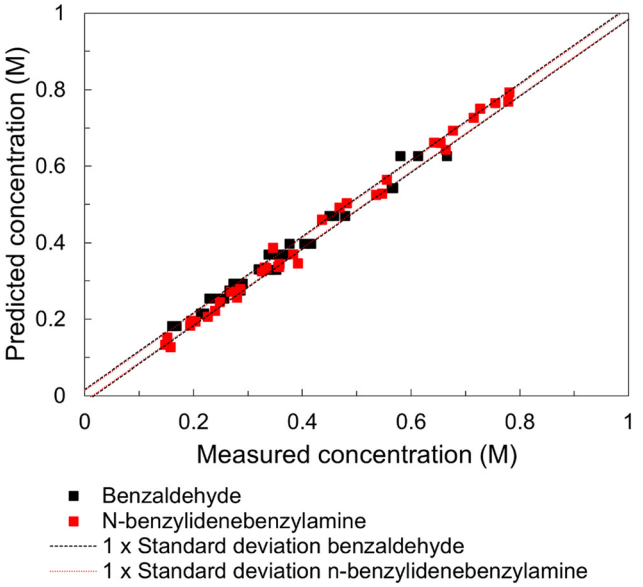

Fig. 8 Parity plot for model predicted and experimentally measured reactor concentrations of benzaldehyde and *n*-benzylidenebenzylamine. The dashed lines represent the one-standard deviation limits.

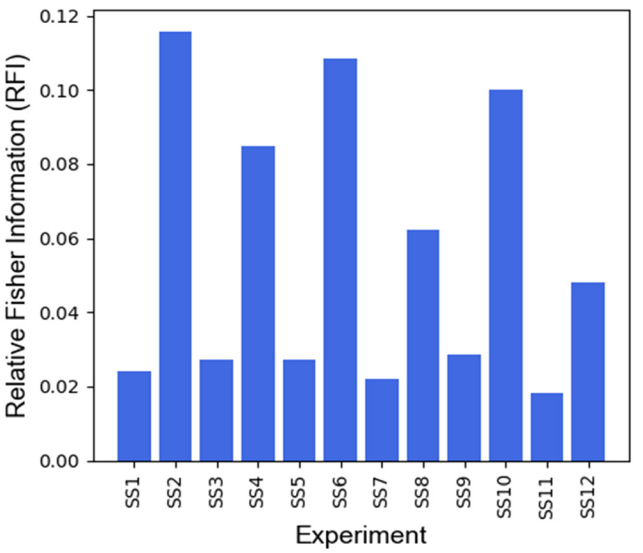

Fig. 9 RFI evaluation for kinetic experiments in the m-CSTR. For the conditions of each experiment refer to Table S3, SI.

Table 3 Comparison of reported kinetic parameters for the synthesis of *n*-benzylidenebenzylamine

Reactor setup	Mode	Temperature (°C)	Residence time (min)	Inlet benzaldehyde concentration (M)	k_{ref} at 25 °C (L mol^{-1} s^{-1})	Activation energy (kJ mol^{-1})
Coiled stainless steel microreactor (Fath *et al.*[42])	Steady-state	15–35	0.2–6	2	0.025–0.065	39.2–43.3
Oscillating segmented flow reactor (Schulz *et al.*[20])	Stopped-flow	15–45	0–5*	0.5–1	0.036–0.037	27.4–29.3
m-CSTR (this work)	Steady-state	15–45	1.2–4.6	0.5–1	0.026	27.5

Note: the asterisk (*) indicates reaction time rather than residence time.

Raman spectroscopy. Similarly to Fath *et al.*,[42] chemometrics were employed to obtain calibration-free kinetic parameters. They reported a reaction rate coefficient of 0.036–0.037 L mol^{-1} s^{-1} at 25 °C and an activation energy in the range of 27.4–29.3 kJ mol^{-1}. The kinetic rate constant and activation energy obtained in our work are of similar magnitude to the ones reported by Fath *et al.*[42] and Schulz *et al.*[20]

4. Conclusions

A miniaturised CSTR (m-CSTR) featuring a stainless-steel chamber with a quartz glass window and an integrated heating jacket was fabricated and was demonstrated for the determination of reaction kinetics of an imine synthesis in continuous flow, employing *in situ* Raman spectroscopy for real-time monitoring. A custom-designed slotted impeller ensured nearly ideal CSTR behaviour and improved micromixing performance when compared to a conventional cross-shaped stir bar. The kinetic parameters of the second order *n*-benzylidenebenzylamine synthesis from benzaldehyde and benzylamine in methanol were determined using Raman spectral data obtained directly from inside the m-CSTR. The flexibility of window selection and easy replacement makes the reactor suitable not only for Raman spectroscopy but also for other spectroscopic techniques. The capability of the reactor to operate as a stirred flow cell further expands its applicability for monitoring reactions involving solid formation/suspension, such as crystallisation reactions.

Author contributions

Eleni Grammenou: writing – original draft, conceptualisation, methodology, software, investigation, formal analysis, data curation. Andrea Friso: writing – original draft, software, methodology, formal analysis, data curation. Simon Dawes: methodology. Nicholas Snead: software. Georgios Gkogkos: software, formal analysis. Maximilian Besenhard: software. Maria Mourkou: methodology. Asterios Gavriilidis: conceptualisation, writing – review & editing, supervision. Federico Galvanin: writing – review & editing, supervision.

Conflicts of interest

There are no conflicts to declare.

Data availability

Supplementary information: The SI provides details on reactor components, Raman probe integration, LabVIEW water circulator control, Raman spectra processing and calibration, RTD and micromixing analysis, flow characterisation, experimental design and statistical analysis. See DOI: **https://doi.org/10.1039/D5RE00144G**.

Data for this article, including micromixing times and Raman-measured concentrations, are available at the Science Data Bank (**https://doi.org/10.57760/sciencedb.22997**). The code is publicly available at: **https://github.com/AndreaFriso/Design-characterisation-and-application-of-a-miniaturised-CSTR**.

Acknowledgements

E. G. thanks EPSRC for her DTP studentship (EP/R513143/1) and Bodossakis Foundation for financial support.

References

1 F. Benito-Lopez, W. Verboom, M. Kakuta, J. G. E. Gardeniers, R. J. M. Egberink, E. R. Oosterbroek, A. van den Berg and D. N. Reinhoudt, *Chem. Commun.*, 2005, 2857–2859.
2 N. Zaborenko, M. W. Bedore, T. F. Jamison and K. F. Jensen, *Org. Process Res. Dev.*, 2011, **15**, 131–139.
3 T. Salmi, J. Hernández Carucci, M. Roche, K. Eränen, J. Wärnå and D. Murzin, *Chem. Eng. Sci.*, 2013, **87**, 306–314.
4 N. Joshi and A. Lawal, *Ind. Eng. Chem. Res.*, 2013, **52**, 4049–4058.
5 C. J. Taylor, M. Booth, J. A. Manson, M. J. Willis, G. Clemens, B. A. Taylor, T. W. Chamberlain and R. A. Bourne, *Chem. Eng. J.*, 2021, **413**, 127017.
6 S. G. Bawa, A. Pankajakshan, C. Waldron, E. Cao, F. Galvanin and A. Gavriilidis, *Chem.: Methods*, 2023, **3**, e202200049.
7 Z. Yan, J. Tian, C. Du, J. Deng and G. Luo, *Chin. J. Chem. Eng.*, 2022, **41**, 49–72.
8 S. K. Ajmera, M. W. Losey, K. F. Jensen and M. A. Schmidt, *AIChE J.*, 2001, **47**, 1639–1647.
9 C. Waldron, A. Pankajakshan, M. Quaglio, E. Cao, F. Galvanin and A. Gavriilidis, *React. Chem. Eng.*, 2019, **4**, 1623–1636.
10 E. Agunloye, P. Petsagkourakis, M. Yusuf, R. Labes, T. Chamberlain, F. L. Muller, R. A. Bourne and F. Galvanin, *React. Chem. Eng.*, 2024, **9**, 1859–1876.

11 B. A. Rizkin, F. G. Popovic and R. L. Hartman, *J. Vac. Sci. Technol., A*, 2019, **37**, 050801.
12 N. Al-Rifai, E. Cao, V. Dua and A. Gavriilidis, *Curr. Opin. Chem. Eng.*, 2013, **2**, 338–345.
13 J. Yue, J. C. Schouten and T. A. Nijhuis, *Ind. Eng. Chem. Res.*, 2012, **51**, 14583–14609.
14 A. Orlando, F. Franceschini, C. Muscas, S. Pidkova, M. Bartoli, M. Rovere and A. Tagliaferro, *Chemosensors*, 2021, **9**, 262.
15 P. J. Aarnoutse and J. A. Westerhuis, *Anal. Chem.*, 2005, **77**, 1228–1236.
16 S. Schwolow, F. Braun, M. Rädle, N. Kockmann and T. Röder, *Org. Process Res. Dev.*, 2015, **19**, 1286–1292.
17 E. Cao, G. Brett, P. J. Miedziak, J. M. Douthwaite, S. Barrass, P. F. McMillan, G. J. Hutchings and A. Gavriilidis, *Catal. Today*, 2017, **283**, 195–201.
18 T. Klement, N. Kockmann and T. Röder, *Chem. Ing. Tech.*, 2019, **91**, 651–656.
19 T. Klement, N. Kockmann, C. Schwede and T. Röder, *Ind. Eng. Chem. Res.*, 2021, **60**, 4240–4250.
20 L. Schulz, P. Stähle, S. Reining, M. Sawall, N. Kockmann and T. Röder, *J. Flow Chem.*, 2023, **13**, 13–19.
21 Y. Mo and K. F. Jensen, *React. Chem. Eng.*, 2016, **1**, 501–507.
22 A. Pomberger, Y. Mo, K. Y. Nandiwale, V. L. Schultz, R. Duvadie, R. I. Robinson, E. I. Altinoglu and K. F. Jensen, *Org. Process Res. Dev.*, 2019, **23**, 2699–2706.
23 I. Lignos, H. Ow, J. P. Lopez, D. A. McCollum, H. Zhang, J. Imbrogno, Y. Shen, S. Chang, W. Wang and K. F. Jensen, *ACS Appl. Mater. Interfaces*, 2020, **12**, 6699–6706.
24 I. Lignos, Y. Mo, L. Carayannopoulos, M. Ginterseder, M. G. Bawendi and K. F. Jensen, *React. Chem. Eng.*, 2021, **6**, 459–464.
25 G. Gkogkos, L. Storozhuk, J. Piovesan, M. R. Penny, S. T. Hilton, N. T. K. Thanh and A. Gavriilidis, *Chem. Eng. Sci.*, 2024, **294**, 120081.
26 G. Gkogkos, E. E. Kahil, L. Storozhuk, N. T. K. Thanh and A. Gavriilidis, *Chem. Eng. Process.: Process Intensif.*, 2024, **203**, 109880.
27 Y. Mo, H. Lin and K. F. Jensen, *Chem. Eng. J.*, 2018, **335**, 936–944.
28 Y. Feng, J. Wang, H. Zhang, J. Wang and Y. Yang, *Green Chem.*, 2021, **23**, 4087–4094.
29 M. R. Chapman, M. H. T. Kwan, G. King, K. E. Jolley, M. Hussain, S. Hussain, I. E. Salama, C. González Niño, L. A. Thompson, M. E. Bayana, A. D. Clayton, B. N. Nguyen, N. J. Turner, N. Kapur and A. J. Blacker, *Org. Process Res. Dev.*, 2017, **21**, 1294–1301.
30 M. Baumann, T. S. Moody, M. Smyth and S. Wharry, *Org. Process Res. Dev.*, 2020, **24**, 1802–1813.
31 J. Yu, J. Liu, C. Li, J. Huang, Y. Zhu and H. You, *Chem. Commun.*, 2024, **60**, 3217–3225.
32 J.-M. Lu, J.-Z. Pan, Y.-M. Mo and Q. Fang, *Artif. Intell. Chem.*, 2024, **2**, 100057.
33 F. Guan, N. Kapur, L. Sim, C. J. Taylor, J. Wen, X. Zhang and A. J. Blacker, *React. Chem. Eng.*, 2020, **5**, 1903–1908.
34 D. Rossi, L. Gargiulo, G. Valitov, A. Gavriilidis and L. Mazzei, *Chem. Eng. Res. Des.*, 2017, **120**, 159–170.
35 T. Huddle, P. Langston and E. Lester, *Int. J. Chem. React. Eng.*, 2018, **16**, 20160219.
36 P. Guichardon and L. Falk, *Chem. Eng. Sci.*, 2000, **55**, 4233–4243.
37 M. O. Besenhard, R. Baber, A. P. LaGrow, L. Mazzei, N. T. K. Thanh and A. Gavriilidis, *CrystEngComm*, 2018, **20**, 7082–7093.
38 J.-M. Commenge and L. Falk, *Chem. Eng. Process.: Process Intesif.*, 2011, **50**, 979–990.
39 J. Villermaux and L. Falk, *Chem. Eng. Sci.*, 1994, **49**, 5127–5140.
40 L. Falk and J.-M. Commenge, *Chem. Eng. Sci.*, 2010, **65**, 405–411.
41 V. Sans, L. Porwol, V. Dragone and L. Cronin, *Chem. Sci.*, 2015, **6**, 1258–1264.
42 V. Fath, P. Lau, C. Greve, N. Kockmann and T. Röder, *Org. Process Res. Dev.*, 2020, **24**, 1955–1968.
43 C. Elliott, V. Vijayakumar, W. Zink and R. Hansen, *JALA*, 2007, **12**, 17–24.
44 Z.-M. Zhang, S. Chen and Y.-Z. Liang, *Analyst*, 2010, **135**, 1138–1146.
45 G. Buzzi-Ferraris and F. Manenti, *Chem. Eng. Sci.*, 2009, **64**, 1061–1074.
46 R. E. Walpole, R. H. Myers, S. L. Myers and K. Ye, *Probability and statistics for engineers and scientists*, Macmillan, New York, 1993.
47 S. D. Silvey, *Statistical inference*, Routledge, New York, 2017.
48 F. Galvanin, C. Psyrraki, T. Morris and A. Gavriilidis, *Chem. Eng. J.*, 2017, **329**, 25–34.
49 F. Galvanin, E. Cao, N. Al-Rifai, A. Gavriilidis and V. Dua, *Comput. Chem. Eng.*, 2016, **95**, 202–215.
50 P. R. Killeen, *Psychol. Sci.*, 2005, **16**, 345–353.
51 J. Denton and W. Dawes, *Proc. Inst. Mech. Eng., Part C*, 1998, **213**, 107–124.